Available online at www.sciencedirect.com
SCIENCE DIRECT®
International Journal of Machine Tools & Manufacture 44 (2004) 401–414
INTERNATIONAL JOURNAL OF MACHINE TOOLS & MANUFACTURE DESIGN, RESEARCH AND APPLICATION
www.elsevier.com/locate/ijmatool

Mechanistic identification of specific force coefficients for a general end mill

Janez Gradišek [a,*,1], Martin Kalveram [b], Klaus Weinert [b]

[a] Faculty of Mechanical Engineering, University of Ljubljana, Aškerčeva 6, Ljubljana SI-1000, Slovenia
[b] Department of Machining Technology (ISF), University of Dortmund, Baroper Straße 301, Dortmund D-44227, Germany

Received 21 August 2003; received in revised form 25 September 2003; accepted 15 October 2003

Abstract

The paper presents expressions for semi-empirical mechanistic identification of specific cutting and edge force coefficients for a general helical end mill from milling tests at an arbitrary radial immersion. The expressions are derived for a mechanistic force model in which the total cutting force is described as a sum of the cutting and edge forces. Outer geometry of the end mill is described by a generalized mathematical model valid for a variety of end mill shapes, such as cylindrical, taper, ball, bull nose, etc. The derivations follow a procedure originally proposed for a cylindrical end mill. The procedure itself is improved by including the helix angle in evaluation of the average edge forces. The resulting expressions for the specific force coefficients are verified by simulations and experiments.

Keywords: End milling; Modelling; Force

1. Introduction

Reliable quantitative prediction of cutting forces in milling is essential for prediction of power and torque requirements, machine-tool vibrations, workpiece surface quality and geometrical accuracy, and chatter-free cutting parameters. The cutting force model commonly employed for this purpose is a mechanistic one assuming the cutting force to be proportional to the cross-sectional area of the uncut chip [1]. The proportionality constant is called the specific cutting force coefficient or specific cutting pressure and depends on the cutter geometry, cutting conditions, and workpiece material properties.

Two types of mechanistic cutting force models are found in the machining literature. In the first one, the effects of shearing mechanism due to the chip generating process on the tool's rake face and effects of rubbing and ploughing mechanisms on the flank face are lumped into one specific force coefficient for each cutting force component (tangential, radial, and axial). This model has been used by many researchers [2–4]. Its disadvantage is a considerable variation of the specific force coefficient with the average chip thickness which complicates analytical calculations. In the second model, the shearing and ploughing effects are characterized separately by the respective specific cutting and edge force coefficients [5–8]. Since the coefficients are relatively independent of the average chip thickness this model appears to be more suitable for analytical work [5]. However, there are twice as many coefficients to be determined as in the simplified lumped model.

In this study, the second model is used, with the total cutting force composed of the tangential, radial, and axial components. The specific cutting and edge force coefficients for each force component can either be predicted from the mechanics theory of machining or experimentally determined from cutting tests. Prediction of coefficients is based on mechanics of general oblique cutting and requires knowledge of the fundamental cutting quantities, such as workpiece material

* Corresponding author. Tel.: +386-1-4771-166; fax: +386-1-2518-567.
E-mail address: janez.gradisek@fs.uni-lj.si (J. Gradišek).
[1] Currently as Alexander von Humboldt Research Fellow at ISF.

0890-6955/$ - see front matter © 2003 Elsevier Ltd. All rights reserved.
doi:10.1016/j.ijmachtools.2003.10.001

shear stress, shear angle, and friction coefficient [5]. These quantities have to be estimated from the orthogonal cutting tests, and form an orthogonal database for a given tool–workpiece material pair. Once the orthogonal database has been established, the specific cutting and edge force coefficients can be predicted for any turning, drilling, and milling operation, given the tool edge geometry and the cutting conditions. Orthogonal database is particularly useful for the design of milling cutters, since the coefficients can be predicted before the cutter has been manufactured. When the orthogonal database is not available or the tool has very complex cutting edges, the specific cutting and edge force coefficients have to be identified mechanistically, from the cutting tests with the given tool and workpiece material. The method adopted in the present study requires a set of milling tests at different feed rates but constant radial and axial immersions. Assuming linear dependence of the average force on feed, the coefficients are obtained by equating the analytical expressions for the average cutting and edge forces to their measured counterparts [5]. If the analytical expressions cannot be derived, the coefficients can be estimated empirically, by minimizing the discrepancy between the predicted and measured cutting force dependencies on the tool rotation angle [7,8]. Despite the disadvantage of the required new set of experiments for each tool geometry, the semi-empirical mechanistic approach is relatively quick and quite common in industrial practice and research laboratories.

The main difficulty associated with the mechanistic identification of the specific cutting and edge force coefficients appears to be the derivation of the analytical expressions for the average milling forces from which the expressions for the coefficients are to be obtained. The machining literature available to the authors provides the analytical expressions for the average forces and the coefficients only for the cylindrical end mill [5], which has the simplest outer geometry among a variety of end mills used in the manufacturing industry today. For more complicated end mill geometries, the coefficients have been either predicted from an orthogonal database [6,9] or identified empirically by a least squares fit [7,8].

This paper presents the expressions for estimation of the specific cutting and edge force coefficients for a *general helical end mill*. The derivations follow the procedure outlined in Ref. [5]. Outer geometry of the end mill is described by a generalized mathematical model [9] which is valid for a variety of end mill shapes, such as cylindrical, taper, ball, bull nose, etc. In the final expressions for the coefficients, the geometrical properties of the mill are represented by six constants that can be evaluated analytically for all helical and non-helical end mills modelled, except for the rounded helical end mills, for which three geometric constants need numerical evaluation. The required milling tests can be conducted at an *arbitrary radial immersion*. The immersion conditions of the cut enter the expressions in the form of five constants that are independent of the end mill geometry and can also be evaluated analytically. The derived expressions for the coefficients are verified by simulations and experiments involving various mill shapes.

2. Geometry of a general end mill

A generalized model of the end mill outer geometry was introduced in Ref. [9]. Similarly to the representation used by CAD/CAM systems, the generalized model describes the cutter envelope by seven geometric parameters: D, R, R_r, R_z, α, β, and H (Fig. 1). The parameters are independent of each other, but subject to geometrical constraints that ensure realizable cutter shapes. A variety of end mill shapes can be defined by these parameters. For example, the cylindrical, ball, and bull nose end mills are defined by, $\{D, R, R_r, R_z, \alpha, \beta, H\} = \{D, 0, D/2, 0, 0, 0, H\}$, $\{D, D/2, 0, D/2, 0, 0, H\}$, and $\{D, R, D/2 - R, R, 0, 0, H\}$, respectively.

In order to evaluate the cutting forces acting on the mill, the cutting edge geometry, chip load, and the cutting force components (tangential, radial, and axial) have to be identified at each point along the helical cutting edge. A point P on the cutting edge is characterized by elevation z, radial distance $r(z)$ from the cutter axis, axial immersion angle $\kappa(z)$, and radial lag angle $\psi(z)$ (Fig. 2). The axial immersion angle is defined as the angle between the cutter axis and normal of the cutting edge at point P. The radial lag angle is the angle between the line connecting P to the cutter axis and tangent to the cutting edge at the cutter tip O.

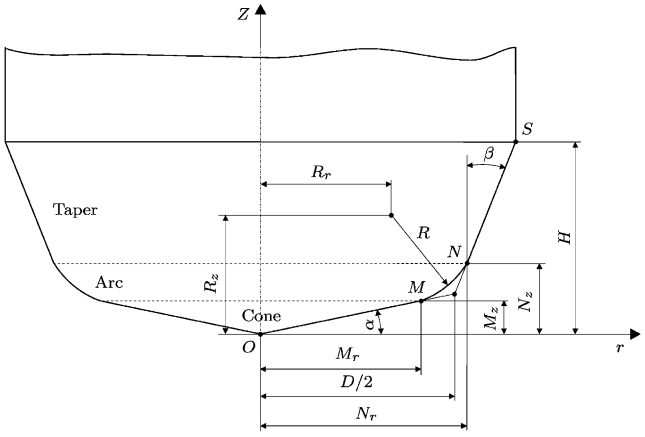

Fig. 1. Geometry of a general end mill. Dashed lines separate three geometrically different zones of the mill.

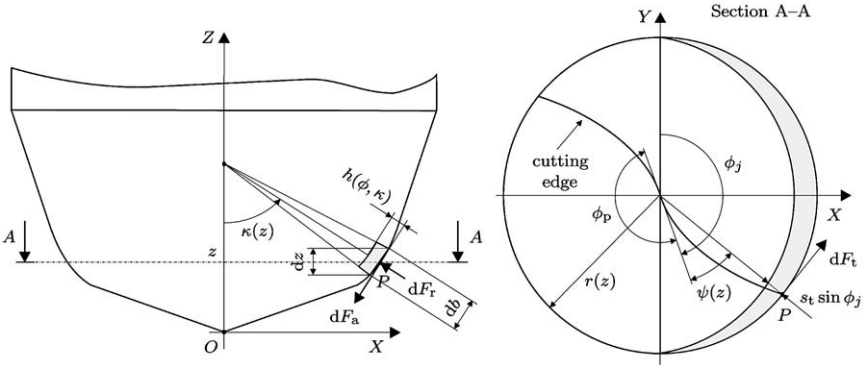

Fig. 2. Chip load, axial immersion angle, radial lag angle, and differential cutting forces at point P.

The location of P on the j-th cutting edge is defined by a vector in cylindrical coordinates as:

$$\mathbf{r}(\phi_j, z) = \mathrm{r}(\phi_j, z)\big(\mathbf{i}\sin\phi_j + \mathbf{j}\cos\phi_j\big) + \mathbf{k}z(\phi_j). \tag{1}$$

The radial immersion angle of the j-th edge varies with elevation z as:

$$\phi_j(z) = \phi + (j-1)\phi_\mathrm{p} - \psi(z), \tag{2}$$

where ϕ denotes the immersion angle of the reference edge ($j = 1$) and $\phi_\mathrm{p} = 2\pi/N$ denotes the pitch angle for a cutter with N uniformly spaced teeth. The expressions for the radial lag angle $\psi(z)$ and distance $r(z)$ depend on the geometry of the cutter envelope.

The envelope of the cutter can be divided into three zones (Fig. 1): (a) the bottom straight part of the cutter (between points O and M), called cone zone, (b) the rounded part of the cutter (between points M and N), called arc zone, and (c) the upper straight part of the cutter (between points N and S), called taper zone. The cutters may have one, two, or all three zones; the cylindrical end mill has only the taper zone, whereas the ball end mill may have both the arc and taper zones, depending on the parameter H, etc. The radial distance, axial immersion angle and radial lag angle dependencies on elevation z in the three zones are as follows [9].

Cone zone, $z \le M_z$:

$$r(z) = \frac{z}{\tan\alpha}, \quad \psi(z) = \frac{\tan\iota_0}{\cos\alpha}\cdot\log\frac{z}{\tan\alpha}, \quad \kappa(z) = \alpha. \tag{3}$$

Arc zone, $M_z < z \le N_z$:

$$r(z) = R_r + R\sqrt{1-(1-E)^2}, \quad \psi(z) = (1-E)\tan\iota_0,$$
$$\kappa(z) = \arcsin\sqrt{1-E^2}, \qquad E(z) = (R_z - z)/R. \tag{4}$$

Taper zone, $N_z < z$:

$$r(z) = N_r + (z - N_z)\tan\beta, \quad \psi^{(0)}(z) = \frac{\tan\iota_0}{\sin\beta}\cdot\log r(z),$$
$$\kappa(z) = \frac{\pi}{2} - \beta, \qquad \psi^{(s)}(z) = \frac{\tan\iota_s}{N_r}(z - N_z). \tag{5}$$

In Eqs. (3)–(5), ι_0 denotes the nominal helix angle, while M_r, M_z, N_r, and N_z denote the cylindrical coordinates of points M and N (Fig. 1). In the taper zone, cutters may be ground with a constant helix angle and variable lead or constant lead and variable helix angle. The lag angles $\psi^{(0)}$ and $\psi^{(s)}$ in Eq. (5) correspond to the former and latter cases, respectively. More detailed description of the local helix and radial lag angle dependencies in the three zones can be found in Ref. [9].

3. Mechanistic cutting force model

The differential tangential (dF_t), radial (dF_r), and axial (dF_a) cutting forces acting on the infinitesimal cutting edge segment are [6]:

$$dF_{\mathrm{t},j}(\phi_j, \kappa) = K_\mathrm{te}dS + K_\mathrm{tc}h(\phi_j, \kappa)db, \tag{6a}$$

$$dF_{\mathrm{r},j}(\phi_j, \kappa) = K_\mathrm{re}dS + K_\mathrm{rc}h(\phi_j, \kappa)db, \tag{6b}$$

$$dF_{\mathrm{a},j}(\phi_j, \kappa) = K_\mathrm{ae}dS + K_\mathrm{ac}h(\phi_j, \kappa)db. \tag{6c}$$

$K_{\cdot\mathrm{c}}$ and $K_{\cdot\mathrm{e}}$ represent the specific cutting and edge force coefficients, respectively. The uncut chip thickness h is measured normal to the cutting edge, and varies along the cutting edge as (Fig. 2):

$$h(\phi_j, \kappa) = s_\mathrm{t}\sin\phi_j\sin\kappa, \tag{7}$$

where s_t denotes feed per tooth. $db = dz/\sin\kappa$ is the chip width. dS is the edge length of the cutting segment which varies with elevation z. dS can be derived from Eq. (1) as:

$$dS = |d\mathbf{r}| = d\phi\sqrt{r^2(\phi) + (r'(\phi))^2 + (z'(\phi))^2}, \tag{8}$$

with $'$ denoting the derivative with respect to ϕ. Taking into account the dependencies of r, ϕ, and ψ on z, the differential edge length is given by:

$$\mathrm{d}S(z) = \mathrm{d}z\sqrt{(r(z)\psi'(z))^2+(r'(z))^2+1}, \tag{9}$$

where $'$ now denotes the derivative with respect to z. The differential forces are thus functions of radial immersion angle ϕ and elevation z:

$$\mathrm{d}F_{\mathrm{t},j}(\phi_j, z) = K_{\mathrm{te}}\mathrm{d}S(z) + K_{\mathrm{tc}}s_{\mathrm{t}}\sin\phi_j\mathrm{d}z, \tag{10a}$$

$$\mathrm{d}F_{\mathrm{r},j}(\phi_j, z) = K_{\mathrm{re}}\mathrm{d}S(z) + K_{\mathrm{rc}}s_{\mathrm{t}}\sin\phi_j\mathrm{d}z, \tag{10b}$$

$$\mathrm{d}F_{\mathrm{a},j}(\phi_j, z) = K_{\mathrm{ae}}\mathrm{d}S(z) + K_{\mathrm{ac}}s_{\mathrm{t}}\sin\phi_j\mathrm{d}z. \tag{10c}$$

The tangential, radial, and axial forces are resolved in the feed (X), normal (Y), and axial (Z) directions by a transformation:

$$\begin{bmatrix}\mathrm{d}F_{x,j}(\phi_j, z)\\ \mathrm{d}F_{y,j}(\phi_j, z)\\ \mathrm{d}F_{z,j}(\phi_j, z)\end{bmatrix} = \begin{bmatrix}-\cos\phi_j & -\sin\kappa\sin\phi_j & -\cos\kappa\sin\phi_j\\ \sin\phi_j & -\sin\kappa\cos\phi_j & -\cos\kappa\cos\phi_j\\ 0 & \cos\kappa & -\sin\kappa\end{bmatrix} \times \begin{bmatrix}\mathrm{d}F_{\mathrm{t},j}(\phi_j, z)\\ \mathrm{d}F_{\mathrm{r},j}(\phi_j, z)\\ \mathrm{d}F_{\mathrm{a},j}(\phi_j, z)\end{bmatrix}. \tag{11}$$

The forces acting on the j-th cutting edge are obtained by integrating Eq. (11) along the axial depth of cut:

$$F_{.,j}(\phi_j) = \int_{z_1}^{z_2}\mathrm{d}F_{.,j}(\phi_j, z). \tag{12}$$

The integration boundaries z_1 and z_2 depend on the immersion of each cutting edge. Finally, the contributions of all cutting edges are summed in order to obtain the total feed, normal, and axial forces acting on the cutter:

$$F_{.}(\phi) = \sum_{j=1}^{N}F_{.,j}(\phi_j). \tag{13}$$

4. Identification of specific force coefficients

Given the cutter geometry and immersion conditions, only the specific cutting and edge force coefficients remain unknown in the right-hand side of Eq. (10). The coefficients can therefore be determined by equating the measured cutting forces with the corresponding analytical expressions. For this purpose, a procedure outlined in Ref. [5] is adopted here. It is based on equating the measured and analytical average cutting forces per tooth. The analytical expression for the average forces is:

$$\bar{F}_{xyz} = \frac{1}{\phi_{\mathrm{p}}}\int_{\phi_{\mathrm{st}}}^{\phi_{\mathrm{ex}}}\int_{z_1}^{z_2}\mathrm{d}F_{xyz}(\phi, z)\mathrm{d}\phi. \tag{14}$$

where ϕ_{st} and ϕ_{ex} denote the start and exit radial immersion angles, respectively. For convenience, the subscript j has been dropped. The analytical calculations are greatly simplified by assuming the average forces per tooth period to be independent of helix angle so that $\iota_0 = 0$ can be set. However, a simple numerical experiment reveals that the assumption is valid only in the absence of edge forces, i.e. for $K_{.\mathrm{e}} = 0$. As shown below, for $K_{.\mathrm{e}} \neq 0$, it is necessary to consider non-zero helix angle in evaluation of the cutting edge length $\mathrm{d}S$ (Eq. (9)).

In order to derive expressions which relate the average forces and specific cutting and edge force coefficients, Eq. (14) has to be integrated. First, the integration along the elevation z is carried out. Due to $\iota_0 = 0$, the immersion angle ϕ is independent of z (Eq. (2)), and the integration boundaries z_1 and z_2 are independent of ϕ. The instantaneous cutting forces at immersion angle ϕ are:

$$\begin{bmatrix}F_x(\phi)\\ F_y(\phi)\\ F_z(\phi)\end{bmatrix} = \frac{s_{\mathrm{t}}}{2}\begin{bmatrix}-K_{\mathrm{tc}}\sin 2\phi & -2K_{\mathrm{rc}}\sin^2\phi & -2K_{\mathrm{ac}}\sin^2\phi\\ 2K_{\mathrm{tc}}\sin^2\phi & -K_{\mathrm{rc}}\sin 2\phi & -K_{\mathrm{ac}}\sin 2\phi\\ 0 & -2K_{\mathrm{ac}}\sin\phi & 2K_{\mathrm{rc}}\sin\phi\end{bmatrix}\begin{bmatrix}A_1\\ A_2\\ A_3\end{bmatrix} + \begin{bmatrix}-K_{\mathrm{te}}\cos\phi & -K_{\mathrm{re}}\sin\phi & -K_{\mathrm{ae}}\sin\phi\\ K_{\mathrm{te}}\sin\phi & -K_{\mathrm{re}}\cos\phi & -K_{\mathrm{ae}}\cos\phi\\ 0 & -K_{\mathrm{ae}} & K_{\mathrm{re}}\end{bmatrix}\begin{bmatrix}B_1\\ B_2\\ B_3\end{bmatrix}, \tag{15}$$

where the constants $A_.$ and $B_.$ denote the integrals:

$$A_1 = \int_{z_1}^{z_2}\mathrm{d}z, \quad A_2 = \int_{z_1}^{z_2}\sin\kappa(z)\mathrm{d}z, \quad A_3 = \int_{z_1}^{z_2}\cos\kappa(z)\mathrm{d}z, \tag{16a}$$

$$B_1 = \int_{z_1}^{z_2}\mathrm{d}S(z), \; B_2 = \int_{z_1}^{z_2}\sin\kappa(z)\mathrm{d}S(z), \; B_3 = \int_{z_1}^{z_2}\cos\kappa(z)\mathrm{d}S(z). \tag{16b}$$

$A_.$ and $B_.$ represent the influence of cutter geometry on the average cutting and edge forces, respectively, and are therefore called the *geometric constants*. They have

to be evaluated for each zone of the cutter (see Appendix A).

Next, the instantaneous forces are averaged over the radial immersion angle yielding:

$$\begin{bmatrix}\bar{F}_x\\ \bar{F}_y\\ \bar{F}_z\end{bmatrix} = \frac{s_t}{\phi_p}\begin{bmatrix} C_3A_1 & (C_2-C_1)A_2 & (C_2-C_1)A_3\\ -(C_2-C_1)A_1 & C_3A_2 & C_3A_3\\ 0 & -C_5A_3 & C_5A_2\end{bmatrix} \times \begin{bmatrix}K_{tc}\\ K_{rc}\\ K_{ac}\end{bmatrix} + \frac{1}{\phi_p}\begin{bmatrix} -C_4B_1 & C_5B_2 & C_5B_3\\ -C_5B_1 & -C_4B_2 & -C_4B_3\\ 0 & 2C_1B_3 & -2C_1B_2\end{bmatrix}\begin{bmatrix}K_{te}\\ K_{re}\\ K_{ae}\end{bmatrix}, \tag{17}$$

where the *immersion constants* $C_{\cdot}$ contain the terms depending on the immersion angles:

$$C_1 = \frac{1}{2}\phi|_{\phi_{st}}^{\phi_{ex}}, \quad C_2 = \frac{1}{4}\sin 2\phi|_{\phi_{st}}^{\phi_{ex}}, \quad C_4 = \sin\phi|_{\phi_{st}}^{\phi_{ex}}, \quad C_3 = \frac{1}{4}\cos 2\phi|_{\phi_{st}}^{\phi_{ex}}, \quad C_5 = \cos\phi|_{\phi_{st}}^{\phi_{ex}}. \tag{18}$$

Eq. (17) represents the average cutting forces per cutter tooth as a linear function of feed s_t:

$$\bar{F}_{\cdot} = \bar{F}_{\cdot c}s_t + \bar{F}_{\cdot e}. \tag{19}$$

$\bar{F}_{\cdot c}$ and $\bar{F}_{\cdot e}$ can be obtained experimentally from milling tests conducted at a series of feeds s_t but constant radial and axial immersions. $\bar{F}_{\cdot c}$ and $\bar{F}_{\cdot e}$ correspond respectively to the slopes and intercepts of the straight lines which approximate the dependence of the measured average cutting forces on feed.

Finally, by equating Eqs. (17) and (19), two systems of linear equations are obtained, whose solutions are the specific cutting and edge force coefficients, $K_{\cdot c}$ and $K_{\cdot e}$:

$$K_{tc} = \frac{2\pi}{NA_1}\cdot\frac{C_3\bar{F}_{xc} - (C_2-C_1)\bar{F}_{yc}}{C_3^2 + (C_2-C_1)^2}, \tag{20a}$$

$$K_{rc} = \frac{2\pi}{N\left(A_2^2+A_3^2\right)} \times \left[\frac{A_2\left((C_2-C_1)\bar{F}_{xc} + C_3\bar{F}_{yc}\right)}{C_3^2+(C_2-C_1)^2} - \frac{A_3\bar{F}_{zc}}{C_5}\right], \tag{20b}$$

$$K_{ac} = \frac{2\pi}{N\left(A_2^2+A_3^2\right)} \times \left[\frac{A_3\left((C_2-C_1)\bar{F}_{xc} + C_3\bar{F}_{yc}\right)}{C_3^2+(C_2-C_1)^2} + \frac{A_2\bar{F}_{zc}}{C_5}\right], \tag{20c}$$

$$K_{te} = \frac{-2\pi}{NB_1}\cdot\frac{C_4\bar{F}_{xe} + C_5\bar{F}_{ye}}{C_4^2+C_5^2}, \tag{21a}$$

$$K_{re} = \frac{2\pi}{N\left(B_2^2+B_3^2\right)} \times \left[\frac{B_2\left(C_5\bar{F}_{xe} - C_4\bar{F}_{ye}\right)}{C_4^2+C_5^2} + \frac{B_3\bar{F}_{ze}}{2C_1}\right], \tag{21b}$$

$$K_{ac} = \frac{2\pi}{N\left(B_2^2+B_3^2\right)} \times \left[\frac{B_3\left(C_5\bar{F}_{xe} - C_4\bar{F}_{ye}\right)}{C_4^2+C_5^2} - \frac{B_2\bar{F}_{ze}}{2C_1}\right]. \tag{21c}$$

It follows from these expressions that the tangential force coefficients $K_{t\cdot}$ are not influenced by the forces in Z direction. The expressions for K_{ac} (K_{ae}) can be derived from K_{rc} (K_{re}) simply by reversing the sign in front of $\bar{F}_{z\cdot}$, and switching the constants A_2 and A_3 (B_2 and B_3).

Using Eqs. (20) and (21), the specific cutting and edge force coefficients can be determined for a general end mill from cutting tests at an arbitrary radial immersion. As noted already in Ref. [5], the simplest expressions for the coefficients with respect to the radial immersion are obtained for slotting, $\phi_{st} = 0$ and $\phi_{ex} = \pi$, where $C_1 = \pi/2$, $C_2 = C_3 = C_4 = 0$, $C_5 = -2$. With respect to the cutter envelope, the simplest coefficients are found for the cylindrical end mill, where $A_1 = A_2 = a$, $B_1 = B_2 = a/\cos\iota_0$, $A_3 = B_3 = 0$, and a is the cutting depth used in the milling tests. Substituting these constants into Eqs. (20) and (21), the same expressions for $K_{\cdot c}$ are obtained as in Ref. [5], whereas $K_{\cdot e}$ differ by a factor $\cos\iota_0$ due to the helix angle.

5. Simulation and experimental results

5.1. Simulations

The derived expressions for the specific cutting and edge force coefficients were first verified using simulated data generated by numerical integration of Eq. (12). The coefficients used in the simulations were calculated from the orthogonal database for a Ti_6Al_4V titanium alloy provided in Refs. [5,10]. The simulations were performed for various cutter geometries covering all three zones of the cutter envelope. In the following, the results are presented for cylindrical, ball, and general end mills (Table 1).

5.1.1. Cylindrical end mill

Envelope of the cylindrical end mill has only the taper zone for which the geometric constants are given by Eq. (A.8). The average cutting forces per tooth were evaluated for a set of five feeds $s_t = \{0.04, 0.08, 0.12, 0.16, 0.2\}$ mm/tooth at the cutting depth $a = 4$ mm. The theoretical coefficients $K_{\cdot c}$

Table 1
Geometry of end mills used in simulations. α_r denotes the rake angle

End mill	D (mm)	R (mm)	R_r (mm)	R_z (mm)	α (°)	β (°)	H (mm)	N (–)	ι_0 (°)	α_r (°)
Cylindrical	8	0	4	0	0	0	20	2	45	0
Ball	8	4	0	4	0	0	20	2	20	12
General	8	2.8	1.6	3.5	20	10	20	2	30	10

predicted from the orthogonal database and used in the numerical integration depend on the instantaneous undeformed chip thickness h which varies with immersion angle (Eq. (7)). As a consequence, the predicted $K_{\bullet c}$ also vary with h. However, the estimated $K_{\bullet c}$ are constant and represent the average coefficients needed to generate the average cutting force observed. In order to be able to reliably verify the derived formulae for the coefficients, two numerical experiments were carried out. In the first, the theoretical $K_{\bullet c}$ were kept constant at the average of the predicted values for the five feeds considered, whereas in the second experiment, the theoretical $K_{\bullet c}$ were allowed to vary with undeformed chip thickness. The specific edge force coefficients remained constant for all simulations, $K_{\bullet e} = [24, 43, -3]$ N/mm.

The estimated coefficients $K_{\bullet c}$ and $K_{\bullet e}$ from the two numerical experiments are listed in Tables 2 and 3 for up- and down-milling at various radial immersions. In the case of constant coefficients (Table 2), the agreement between the theoretical and estimated values is excellent for all radial immersions considered. Also shown in Table 2 are the edge coefficients obtained when neglecting the helix angle. As expected, the coefficients are overestimated by a factor of $1/\cos\iota_0 = \sqrt{2}$.

Table 3 shows the estimates in the case of variable theoretical $K_{\bullet c}$, which is a more realistic example. The estimated $K_{\bullet c}$ for different radial immersions are very similar, although they tend to decrease slightly as the radial immersion decreases. The estimated $K_{\bullet e}$ are reasonably close to the corresponding theoretical values, whereby the tangential and axial coefficients are over- and underestimated, respectively. Again, neglecting the helix angle increases the estimated $K_{\bullet e}$ by a factor of $\sqrt{2}$.

To examine the effect of deviations in the estimated $K_{\bullet c}$ on cutting force prediction, the forces in 50% down-milling were predicted using the theoretical variable coefficients and the coefficients obtained from 10% up-milling tests. The resulting force traces (Fig. 3) are practically indistinguishable what indicates that the deviations in $K_{\bullet c}$ and $K_{\bullet e}$ observed in Table 3 are negligible. Also shown in Fig. 3 are the predictions achieved using the zero-helix edge coefficients, $K_{\bullet e,0}$. While the predicted and theoretical force traces match qualitatively, differences are observed in the amplitudes of F_x and F_y.

5.1.2. Ball end mill

Envelope of the ball end mill consists of the arc and taper zones (Table 1). In contrast to the cone and taper zones, axial immersion angle κ within the arc zone varies along the cutter axis. Since the specific cutting force coefficients depend on κ, a series of cutting depths has to be considered in experiments for the variation of $K_{\bullet c}$ with κ to be determined. For this purpose, the cutting depths from 0.04 to 5.0 mm at 0.04 mm increments were used in the simulations. For $a \leq 4$ mm, only the arc zone of the mill is engaged in the cut, while for $4 < a \leq 5$ mm, the entire arc zone and part of the taper zone are cutting. The average cutting forces per tooth were calculated for the same set of feeds as for the cylindrical end mill.

Fig. 4 shows the variation of the estimated $K_{\bullet c}$ and $K_{\bullet e}$ with cutting depth for down-milling tests at various radial immersions. The results for up-milling are similar. The tangential and radial cutting force coefficients increase slightly after an initial decrease, whereas the axial cutting force coefficient increases monotonously and significantly. As expected, $K_{\bullet c}$ reach their limit

Table 2
Estimated $K_{\bullet c}$ (in N/mm^2) and $K_{\bullet e}$ (in N/mm) for the cylindrical end mill using constant theoretical $K_{\bullet c} = [1844.1,\ 513.0,\ 1118.7]$ N/mm^2 (see text). $K_{\bullet e,0}$ are obtained for $\iota_0 = 0$

Immersion	K_{tc}	K_{rc}	K_{ac}	K_{te}	K_{re}	K_{ae}	$K_{te,0}$	$K_{re,0}$	$K_{ae,0}$
100%	1844.1	513.0	1118.7	24.0	43.0	−3.0	33.9	60.8	−4.2
50%-down	1843.9	512.8	1118.5	24.0	43.0	−3.0	33.9	60.8	−4.2
50%-up	1844.4	512.9	1118.9	24.0	43.0	−3.0	33.9	60.8	−4.2
25%-down	1844.5	513.3	1119.0	24.0	43.0	−3.0	33.9	60.8	−4.2
25%-up	1844.0	513.0	1118.6	24.0	43.0	−3.0	33.9	60.8	−4.2
10%-down	1844.4	513.2	1118.9	24.0	43.0	−3.0	33.9	60.8	−4.2
10%-up	1843.9	513.0	1118.6	24.0	43.0	−3.0	33.9	60.8	−4.2

Table 3
Estimated $K_{\bullet c}$ (in N/mm^2) and $K_{\bullet e}$ (in N/mm) for the cylindrical end mill using variable theoretical $K_{\bullet c}$ (see text). $K_{\bullet e,0}$ are obtained for $\iota_0 = 0$

Immersion	K_{tc}	K_{rc}	K_{ac}	K_{te}	K_{re}	K_{ae}	$K_{te,0}$	$K_{re,0}$	$K_{ae,0}$
100%	1799.9	500.7	1087.3	26.6	43.7	−1.1	37.6	61.8	−1.6
50%-down	1789.3	509.8	1087.1	27.4	43.2	−1.1	38.8	61.1	−1.6
50%-up	1796.1	487.2	1087.5	27.0	44.6	−1.1	38.2	63.0	−1.6
25%-down	1763.0	493.8	1070.4	28.3	44.1	−0.5	40.0	62.4	−0.7
25%-up	1764.2	487.6	1070.1	28.2	44.3	−0.5	39.9	62.6	−0.7
10%-down	1745.5	481.3	1058.6	28.6	44.5	−0.2	40.5	62.9	−0.3
10%-up	1742.8	489.2	1058.3	28.7	44.1	−0.2	40.6	62.4	−0.3

value at the end of the arc zone, $a = R$, and remain constant in the taper zone, $a > R$. Also shown in Fig. 4 are the average theoretical $K_{\bullet c}$ at $s_t = 0.12$ mm/tooth, evaluated as suggested in Ref. [10]. The agreement between the estimated and theoretical $K_{\bullet c}$ is reasonable for the tangential and radial coefficients and very good for the axial coefficient. Overall, the estimates obtained using different radial immersions agree well. For $a < 0.3$ mm, smaller radial immersions yield larger coefficients than larger immersions, while for $a > 0.3$ mm, the situation is reversed. The largest deviations between the estimates of different immersions are observed for K_{rc}, and lie within ±6% around the mean value. The estimated specific edge force coefficients also vary a little with cutting depth and radial immersion, but nevertheless remain close to the constant theoretical values.

In Fig. 5, the predicted cutting force traces are compared for 50% down-milling at $a = 0.2$ and 4.5 mm. The predictions were made using the theoretical variable coefficients and those estimated from 10% down-milling tests. At $a = 0.2$ mm, the predicted forces agree very well, despite differences between the theoretical average and estimated coefficients. The agreement of the predictions for $a = 4.5$ mm is even better.

5.1.3. General end mill

For the last simulation example, a general end mill with all three zones was devised (Table 1), with 20 mm

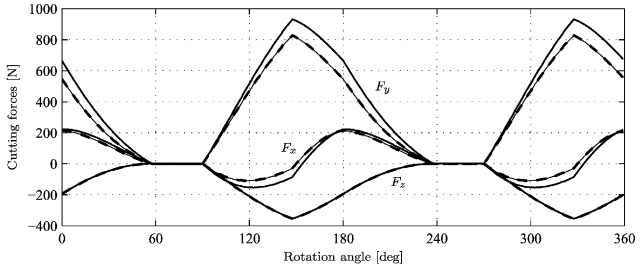

Fig. 3. Comparison of cutting forces for down-milling with the cylindrical end mill; 50% radial immersion, $s_t = 0.1$ mm/tooth, $a = 4$ mm. Lines: predicted using the theoretical coefficients (thin solid), the coefficients estimated from 10% up-milling tests (thick dashed), same as the latter, but with $K_{\bullet e,0}$ (thick solid).

constant lead in the taper zone. Since the specific cutting force coefficients are constant in the cone and taper zones, if suffices to identify their values at one cutting depth per zone. In the arc zone, the coefficients vary with axial immersion so that they have to be determined at a series of cutting depths. The same set of feeds as for the first two examples was used.

Fig. 6 shows the estimates of $K_{\bullet c}$ and $K_{\bullet e}$ from up-milling tests at various radial immersions. As expected, the cutting force coefficients are constant within the cone and taper zones, and vary monotonously within the arc zone. Rather abrupt changes of $K_{\bullet c}$ values are observed at the transitions between the cutter zones. The estimates obtained at the various radial immersions agree well. Again, the specific edge force coefficients are overestimated and vary with cutting depth within the arc zone, but their values are still reasonably near the constant theoretical values.

Finally, the cutting forces for 50% up-milling were predicted using the theoretical and estimated coefficients (10% up-milling). The cutting depth was set to 4 mm so that all three cutter zones were engaged in the cut. The predicted forces from both sets of coefficients are practically indistinguishable (Fig. 7).

5.2. Experiments

For experimental verification of the derived formulae for the specific cutting and edge force coefficients, cylindrical, bull nose, and ball end mills were employed (Table 4). In order to avoid excessive vibration, short mills were used, with overhang to diameter ratio of 4. The workpieces made of aluminum alloy AlMgSi0.5 were machined on a CNC milling center. The cutting forces in the feed, normal, and axial direction were measured by a three-component dynamometer. The signals were low-pass filtered with a cut off frequency of 1 kHz, and sampled at a frequency of 50 kHz. For all experiments, spindle speed was held constant at 4000 rpm, and minimal quantity lubrication was used.

5.2.1. Cylindrical end mill

Specific cutting and edge force coefficients were estimated from 100%, 50%, and 25% radial immersion up-

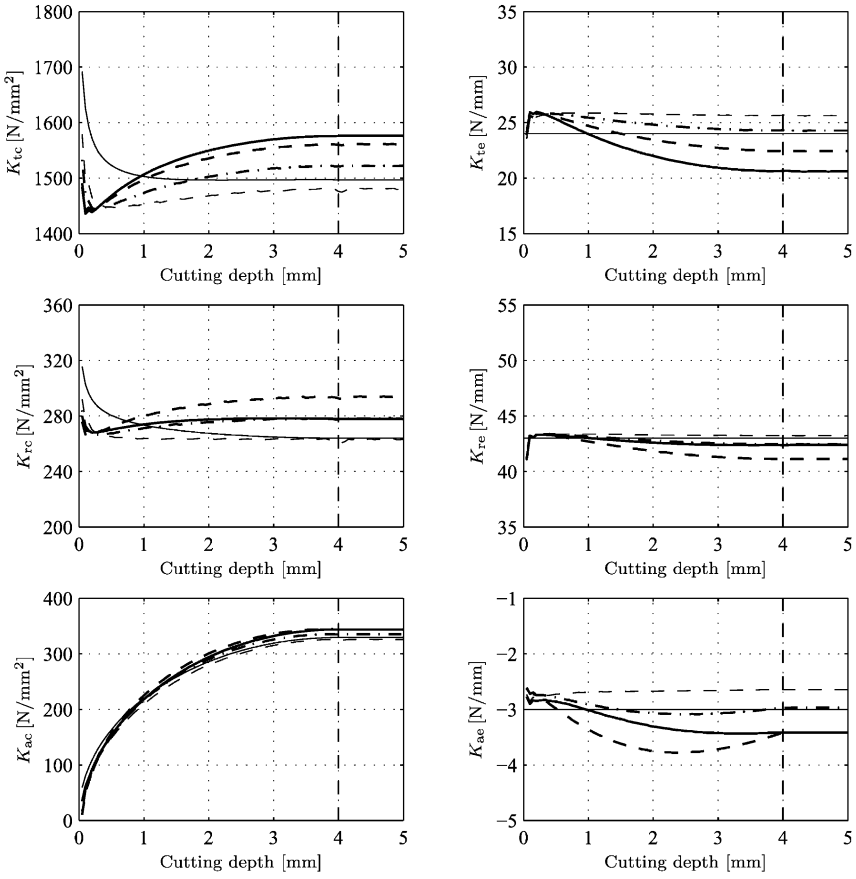

Fig. 4. Estimated $K_{\bullet c}$ and $K_{\bullet e}$ vs. cutting depth for the ball end mill. Lines: 100% radial immersion (thick solid), 50% (thick dashed), 25% (thick dash-dotted), 10% (thin dashed), theoretical average coefficients (thin solid); all down-milling. The vertical dashed line separates the arc and taper zones of the cutter.

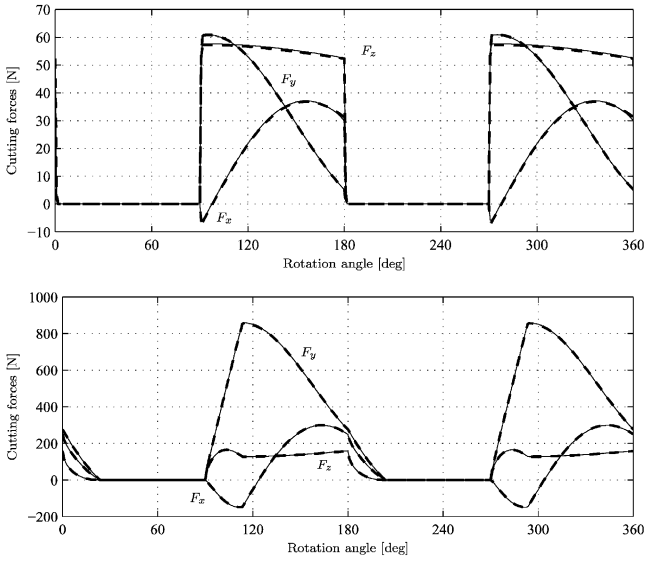

Fig. 5. Comparison of cutting forces for down-milling with the ball end mill; 50% radial immersion, $s_t = 0.1$ mm/tooth, $a = 0.2$ mm (top panel), $a = 4.5$ mm. Lines: predicted using the theoretical coefficients (thin solid) and the coefficients estimated from 10% down-milling tests (thick dashed).

milling tests at a cutting depth $a = 2$ mm and feeds $s_t = \{0.08,\ 0.10,\ 0.12,\ 0.14,\ 0.16\}$ mm/tooth. The tests were repeated four times at each combination of cutting parameters. The mean estimates of $K_{\bullet c}$ and $K_{\bullet e}$ are listed in Table 5. The specific cutting force coefficients $K_{\bullet c}$ obtained from different radial immersions agree well. K_{tc} increases slightly with decreasing immersion, while no such trend is observed for K_{rc} and K_{ac}. The tangential and radial edge force coefficients, K_{te} and K_{re}, decrease markedly as immersion decreases, whereas K_{ae} remains unchanged.

Fig. 8 shows the average measured and predicted cutting force traces for one cutter revolution during 50% up-milling. The average measured traces were averaged over more than 100 cutter revolutions. The predictions and measurements agree very well. A discrepancy is observed mainly in the feed force, F_x, where the larger K_{tc} values estimated from the tests at lower immersions result in smaller force amplitude. Also contributing to the discrepancy between the predicted and measured forces is the cutter runout. A detailed inspection of the measured forces reveals that the force traces corresponding to engagement of the

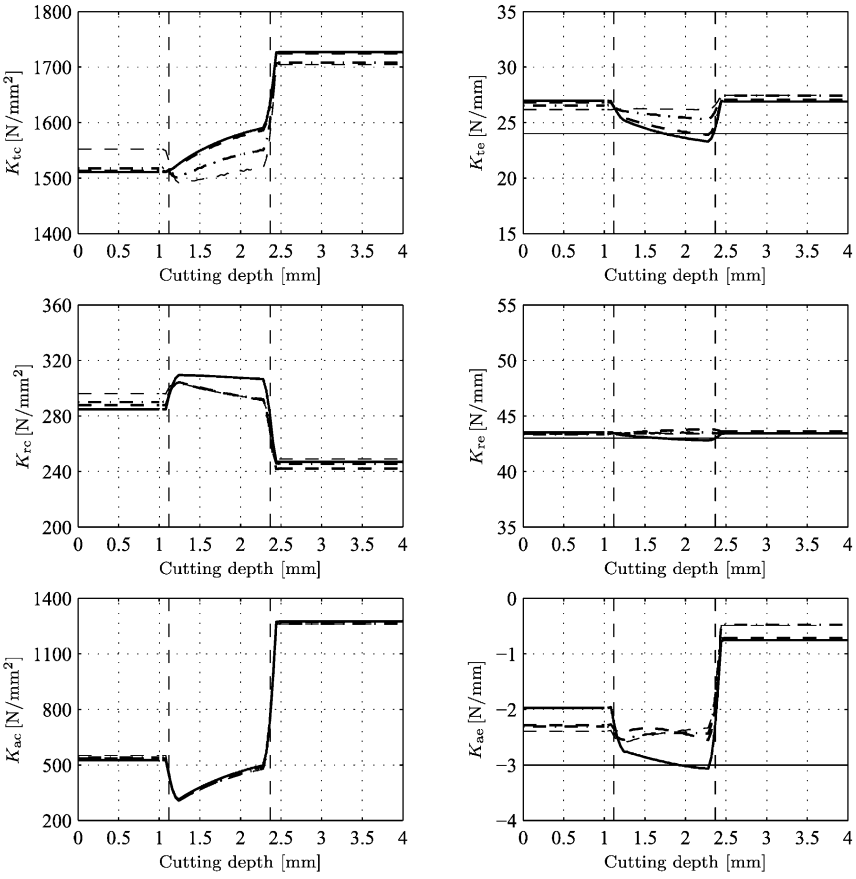

Fig. 6. Estimated $K_{\bullet c}$ and $K_{\bullet e}$ vs. cutting depth for the general end mill. Lines: 100% radial immersion (thick solid), 50% (thick dashed), 25% (thick dash-dotted), 10% (thin dashed); all up-milling. The vertical dashed lines separate the cutter zones.

individual cutting edges differ, what indicates that the two edges are not identical. Also note that the measured forces do not vanish during the non-cutting portion of the cutter revolution period, but fluctuate around zero. Regardless of their cause, these fluctuations affect the mean forces per tooth period and thus distort the estimates of specific force coefficients obtained from milling tests at partial radial immersions.

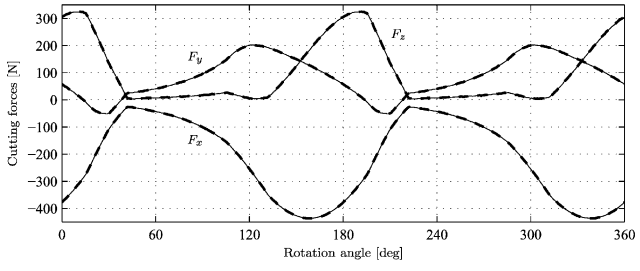

Fig. 7. Comparison of cutting forces for up-milling with the general end mill; 50% radial immersion, $s_t = 0.1$ mm/tooth, $a = 4$ mm. Lines: predicted using the theoretical coefficients (thin solid) and coefficients estimated from 10% up-milling tests (thick dashed).

5.2.2. *Bull nose end mill*

The envelope of the bull nose end mill has two zones, arc and taper. In order to estimate the variation of the specific force coefficients within the arc zone, milling tests were conducted at depths $a = \{0.1, 0.2, 0.44, 0.75, 1.11, 1.5\}$ mm. Except for $a = 0.1$ mm, the depths were chosen such that the increments of the axial immersion angle κ were constant. In the taper zone, $a = 1.75$ and 2 mm were selected. The feeds $s_t = \{0.08, 0.1, 0.12, 0.14, 0.16\}$ mm/tooth were used in both zones. Full immersion and 50% radial immersion up-milling tests were repeated four times at each depth and feed. In the taper zone, however, the full immersion tests were plagued by chatter so that the coefficients were estimated only from the half-immersion tests. Individual estimates were obtained for each of the four repeated tests separately, whereas the average coefficient was estimated by combining the average forces per tooth from all four tests. The results are summarized in Fig. 9. As expected, the estimated specific cutting force coefficients $K_{\bullet c}$ vary significantly with cutting depth. K_{tc} and K_{rc} decrease at small depths and increase towards the end of the arc zone, while K_{ac} increases

Table 4
Geometry of end mills used in experiments

End mill	D (mm)	R (mm)	R_r (mm)	R_z (mm)	α (°)	β (°)	H (mm)	N (–)	ι_0 (°)
Cylindrical	8	0	4	0	0	0	20	2	45
Bull nose	10	1.5	3.5	1.5	0	0	16	2	30
Ball	8	4	0	4	0	0	20	2	30

Table 5
Estimated $K_{\bullet c}$ (in N/mm^2) and $K_{\bullet e}$ (in N/mm) for the cylindrical end mill

Immersion	K_{tc}	K_{rc}	K_{ac}	K_{te}	K_{re}	K_{ae}
100%	561.2	204.3	194.4	16.2	6.7	2.2
50%-up	617.2	235.8	188.3	9.3	1.8	2.4
25%-up	644.5	209.7	196.3	4.2	0.7	2.0

monotonously. In the taper zone, $K_{\bullet c}$ are approximately constant. The specific edge force coefficients $K_{\bullet e}$ exhibit much less variation with cutting depth than $K_{\bullet c}$, although a distinct change of K_{te} and K_{re} is observed between the two zones. The estimates from 100% to 50% immersion tests agree well, except for $a = 0.1$ mm, where the estimate of K_{tc} from the 100% immersion test is much lower than that from the 50% immersion. It can also be observed that scatter of the individual estimates is more pronounced at small depths and it is on average larger for the 50% than for the 100% immersion tests.

In order to enable prediction of cutting forces at depth increments other than those considered in the experiments, the estimated dependence of the average coefficients on cutting depth was approximated by a 4th order polynomial. Examples of predicted force traces using the two sets of estimated coefficients are shown in Fig. 10 for 100% and 50% up-milling at $a = 0.75$ mm. The predicted traces are very similar what confirms that the two sets of coefficients are practically equivalent. Also shown in Fig. 10 are the average measured force traces. The predictions and measurements agree quite well. The discrepancies observed are mainly due to the cutter runout.

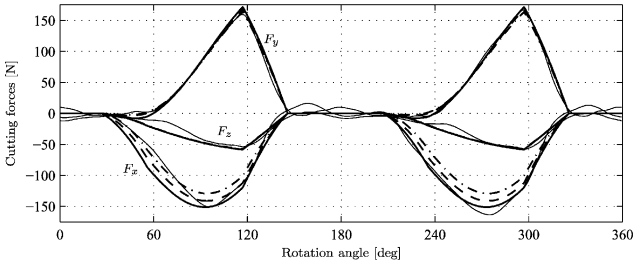

Fig. 8. Comparison of cutting forces for up-milling with the cylindrical end mill; 50% radial immersion, $s_t = 0.14$ mm/tooth, $a = 2.0$ mm. Lines: measured forces (thin solid), predicted forces using coefficients estimated from 100% (thick solid), 50% (thick dashed), and 25% (thick dash-dotted) up-milling tests.

5.2.3. Ball end mill

The ball end mill envelope is also composed of the arc and taper zones. Experiments with 50% radial immersion down-milling were carried out at a series of 11 depths $a = \{0.14, 0.3, 0.54, 0.83, 1.17, 1.56, 2, 2.47, 2.96, 3.48, 4\}$ mm within the arc zone, and at $a = 4.4$ mm in the taper zone. The selected depths from 0.14 mm onwards correspond to constant increments of the axial immersion angle κ in the arc zone. The feeds were $s_t = \{0.08, 0.1, 0.12, 0.14\}$ mm/tooth. The tests were repeated five times at each cutting depth and feed. The individual and mean estimates of the specific force coefficients are shown in Fig. 11. Again, the specific cutting force coefficients vary significantly with cutting depth. The initial decrease of K_{tc} and K_{rc} at small cutting depths is followed by a gradual increase of their values towards the end of the arc zone, whereas K_{ac} increases monotonously throughout the entire arc zone. Despite some local distortions, the average dependencies of $K_{\bullet c}$ on cutting depth are qualitatively in good agreement with those obtained from the simulations (Fig. 4). As expected, no systematic variations of the specific edge force coefficients are observed so that $K_{\bullet e}$ can be considered practically constant.

The estimated dependence of specific force coefficients on cutting depth was approximated by a 4th order polynomial which was then used in predicting the cutting forces. The predictions and measurements are compared in Fig. 12 for $a = 0.54$, 2, and 4 mm. Apart from the cutter runout, the predicted and average measured force traces agree very well. The effect of runout is most expressive in the feed force F_x trace at $a = 0.54$ mm, and it appears to diminish at larger cutting depths. Note that the discrepancy between the predicted and measured axial forces F_z grows with cutting

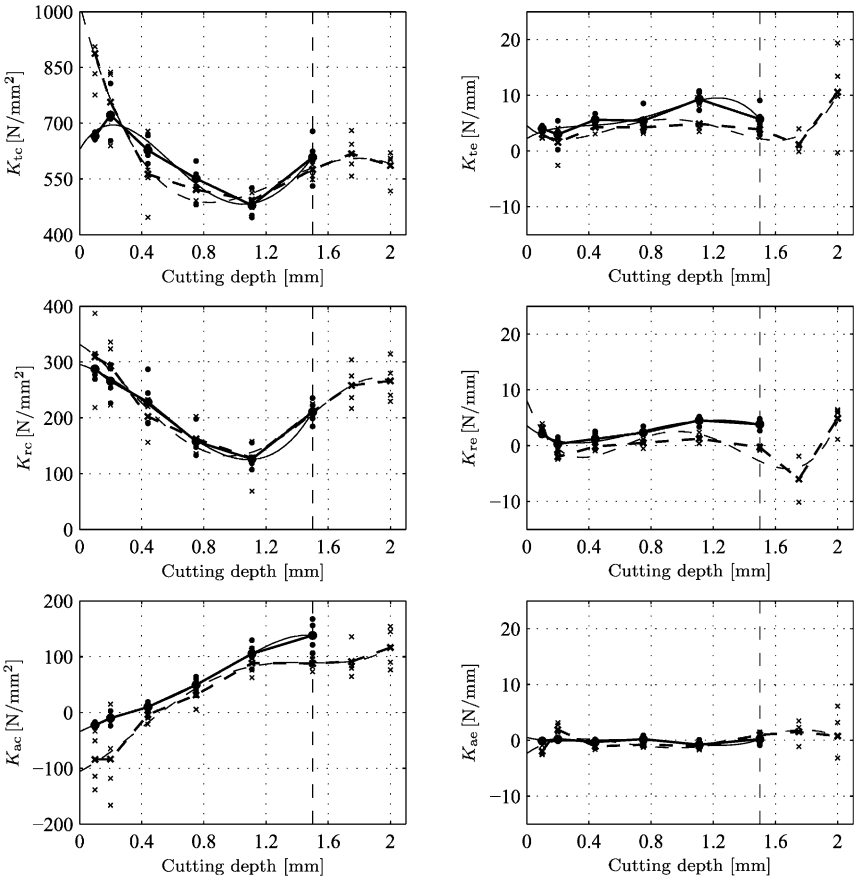

Fig. 9. Estimated $K_{\cdot c}$ and $K_{\cdot e}$ vs. cutting depth for the bull nose end mill. Radial immersion: 100% (circles, solid lines) and 50% up-milling (crosses, dashed lines). Points: individual (small) and average values (large). Lines: estimated dependence (thick) and its 4th order polynomial approximation (thin). The vertical dashed line separates the two cutter zones.

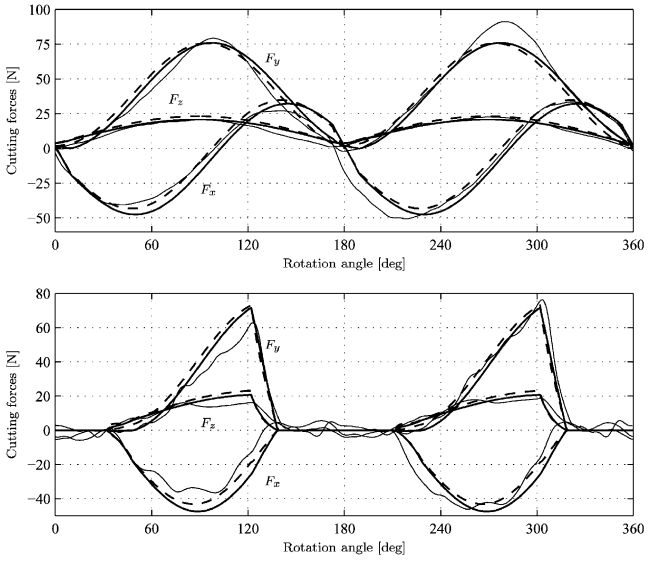

Fig. 10. Comparison of cutting forces for up-milling with the bull nose end mill; 100% (top panel) and 50% radial immersion, $s_t = 0.14$ mm/tooth, $a = 0.75$ mm. Lines: measured forces (thin solid), predicted forces using coefficients estimated from 100% (thick solid) and 50% up-milling tests (thick dashed).

depth. This is presumably caused by the cutter and workpiece–dynamometer vibrations which have the strongest effect on F_z since its amplitude is relatively small. Cutting forces predicted using constant specific force coefficients obtained from the tests at $a = 0.54$ mm are also shown in Fig. 12. These predictions agree well with the measured forces only at depths close to $a = 0.54$ mm. The more the depth used in predictions differs from the depth used to estimate the constant coefficients, the larger the discrepancy between the predicted and measured forces. As noted already in Ref. [10], if the variable specific force coefficients are not available, the constant coefficients estimated at the half of the arc zone should provide reasonable predictions across the entire arc zone.

6. Conclusions

The expressions for semi-empirical mechanistic identification of specific cutting and edge force coefficients for a general helical end mill from milling

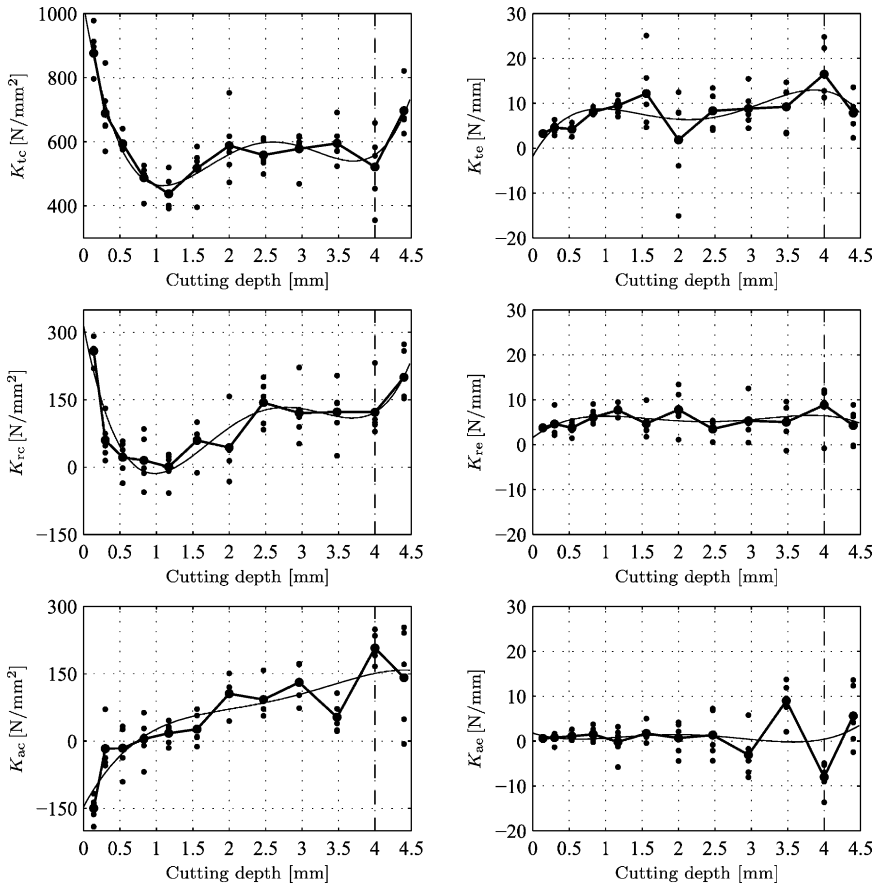

Fig. 11. Estimated $K_{\bullet c}$ and $K_{\bullet e}$ vs. cutting depth for the ball end mill. Radial immersion: 50% down-milling. Points: individual (small) and average values (large). Lines: estimated dependence (thick) and its 4th order polynomial approximation (thin). The vertical dashed line separates the two cutter zones.

tests at an arbitrary radial immersion were presented in the paper. The expressions are based on the commonly used mechanistic cutting force model which describes the total cutting force as a sum of the cutting (shearing) and edge (ploughing) forces. The outer geometry of the end mill was described by a generalized mathematical model. Derivation of the analytical expressions for the average cutting forces per tooth period followed the procedure proposed in Ref. [5]. The procedure was improved by considering non-zero helix angle in evaluation of the average edge forces. By equating the analytical and measured average forces, expressions for the specific cutting and edge force coefficients were obtained. In these expressions, the end mill geometry and the radial immersion conditions are represented by six and five constants, respectively. The constants can be evaluated analytically for all non-helical and almost all helical end mills modelled. The exception are the rounded helical mills, for which three geometric constants have to be calculated numerically.

The derived expressions were verified by simulations and experiments involving various end mill shapes and radial immersions. The simulation examples confirmed validity of the expressions and also showed that taking non-zero helix angle into account improves the estimates of the edge force coefficients. The experimental examples revealed that milling tests at various radial immersions can result in moderately different estimates of the force coefficients. The main reason for the deviations appear to be the fluctuations of the cutting forces recorded in the non-cutting portions of the tool revolution period in partial immersion milling where no tool–workpiece contact is expected and the cutting forces should be zero. The fluctuations were probably caused by tool and/or workpiece–dynamometer vibrations, they had much smaller amplitude than the forces during cutting, and were therefore insignificant in the full immersion milling. However, full immersion milling is more vulnerable to chatter vibrations so that in cases when variation of the coefficients with axial immersion angle is to be determined, partial radial immersions may be the only alternative.

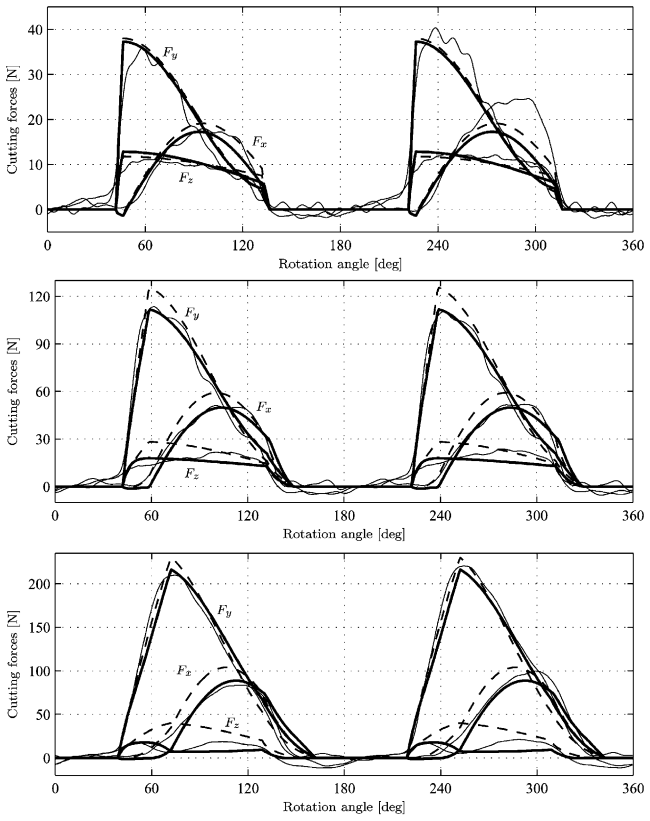

Fig. 12. Comparison of cutting forces for down-milling with the ball end mill; 50% radial immersion, $s_t = 0.08$ mm/tooth, $a = 0.54$ mm (top panel), $a = 2.0$ mm (middle panel), $a = 4.0$ mm. Lines: measured forces (thin solid), predicted forces using the estimated variable coefficients (thick solid) and constant coefficients estimated from the tests at $a = 0.54$ mm (thick dashed).

The main contributions of this paper can be summarized as: (1) the expressions for the semi-empirical mechanistic identification of the specific cutting and edge force coefficients were derived for a general end mill. This extends the applicability of the identification method from the geometrically simplest, cylindrical end mill to a variety of end mill shapes describable by the employed generalized mathematical model, such as ball, bull nose, taper, taper ball, etc. (2) The derived expressions take non-zero helix angle into account which significantly improves the estimates of the edge force coefficients. (3) The milling tests required by the procedure can be conducted at an arbitrary radial immersion for any cutter geometry considered.

Acknowledgements

JG gratefully acknowledges the support of the Alexander von Humboldt Foundation.

Appendix A. Geometric constants for the cutter zones

The geometric constants $A_.$ and $B_.$ are defined by Eq. (16) which is repeated here for convenience:

$$A_1 = \int_{z_1}^{z_2} \mathrm{d}z, \quad A_2 = \int_{z_1}^{z_2} \sin\kappa(z)\mathrm{d}z, \quad A_3 = \int_{z_1}^{z_2} \cos\kappa(z)\mathrm{d}z, \tag{A.1a}$$

$$B_1 = \int_{z_1}^{z_2} \mathrm{d}S(z), B_2 = \int_{z_1}^{z_2} \sin\kappa(z)\mathrm{d}S(z), B_3 = \int_{z_1}^{z_2} \cos\kappa(z)\mathrm{d}S(z). \tag{A.1b}$$

The expressions for $A_.$ and $B_.$ in the three cutter zones are given in the following.

A.1. Cone zone, $z < M_z$

The differential edge length is:

$$\mathrm{d}S(z) = \frac{\mathrm{d}z}{\cos\iota_0 \sin\alpha}. \tag{A.2}$$

The geometric constants are:

$$A_1 = z|_{z_1}^{z_2}, \quad A_2 = \sin\alpha \cdot z|_{z_1}^{z_2}, \quad A_3 = \cos\alpha \cdot z|_{z_1}^{z_2}, \tag{A.3a}$$

$$B_1 = \frac{1}{\cos\iota_0 \sin\alpha} \cdot z|_{z_1}^{z_2}, \quad B_2 = \frac{1}{\cos\iota_0} \cdot z|_{z_1}^{z_2}, \quad B_3 = \frac{\mathrm{ctg}\alpha}{\cos\iota_0} \cdot z|_{z_1}^{z_2}. \tag{A.3b}$$

A.2. Arc zone, $M_z < z \le N_z$

The differential edge length is:

$$\mathrm{d}S(z) = \mathrm{d}z\sqrt{\tan^2\iota_0\left(\frac{R_r}{R} + \sqrt{1-E^2}\right)^2 + \frac{1}{1-E^2}}, \tag{A.4}$$

with $E(z) = (R_z - z)/R$. The geometric constants are:

$$\begin{aligned} A_1 &= z|_{z_1}^{z_2}, \\ A_2 &= -\frac{R}{2}\left(E\sqrt{1-E^2} + \arcsin E\right)\Big|_{z_1}^{z_2}, \\ A_3 &= \frac{1}{R}\left(R_z z - \frac{z^2}{2}\right)\Big|_{z_1}^{z_2}, \end{aligned} \tag{A.5a}$$

$$\begin{aligned} B_1 &= \int_{z_1}^{z_2} \mathrm{d}z\sqrt{\tan^2\iota_0\left(\frac{R_r}{R} + \sqrt{1-E^2}\right)^2 + \frac{1}{1-E^2}}, \\ B_2 &= \int_{z_1}^{z_2} \mathrm{d}z\sqrt{\tan^2\iota_0\left(\frac{R_r}{R} + \sqrt{1-E^2}\right)^2 (1-E^2) + 1}, \\ B_3 &= \int_{z_1}^{z_2} E\mathrm{d}z\sqrt{\tan^2\iota_0\left(\frac{R_r}{R} + \sqrt{1-E^2}\right)^2 + \frac{1}{1-E^2}}. \end{aligned} \tag{A.5b}$$

The integrals for $B_.$ have to be evaluated numerically. In the case of non-helical ball end mill, $\iota_0 = 0$,

the differential edge length is $dS(z) = dz/\sqrt{1-E^2}$, and $B_.$ can be determined analytically:

$$B_1 = -R\arcsin E|_{z_1}^{z_2},\ B_2 = z|_{z_1}^{z_2},\ B_3 = R\sqrt{1-E^2}\Big|_{z_1}^{z_2}. \quad \text{(A.6)}$$

A.3. Taper zone, $N_z < z$

If the cutter is ground with constant helix angle ι_0 and variable lead L, the differential edge length is

$$dS(z) = \frac{dz}{\cos\iota_0\cos\beta}. \quad \text{(A.7)}$$

The geometric constants are:

$$A_1 = z|_{z_1}^{z_2},\quad A_2 = \cos\beta\cdot z|_{z_1}^{z_2},\quad A_3 = \sin\beta\cdot z|_{z_1}^{z_2}, \quad \text{(A.8a)}$$

$$B_1 = \frac{1}{\cos\iota_0\cos\beta}\cdot z|_{z_1}^{z_2},\quad B_2 = \frac{1}{\cos\iota_0}\cdot z|_{z_1}^{z_2},\quad B_3 = \frac{\tan\beta}{\cos\iota_0}\cdot z|_{z_1}^{z_2}. \quad \text{(A.8b)}$$

If the cutter is ground with constant lead L, the helix angle ι varies with elevation z. Denoting the nominal helix angle by ι_s, the differential edge length is:

$$dS(z) = \frac{dz}{\cos\beta}\sqrt{(F/G)^2+1}, \quad \text{(A.9)}$$

with $F = r(z)/\tan\beta$ and $G = L/(2\pi\tan\beta)$. The cutting geometric constants $A_.$ are the same as for the constant helix case (Eq. (A.8a)), while the edge geometric constants are:

$$B_1 = \frac{1}{2G\cos\beta}\left(F\sqrt{G^2+F^2} + G^2\log\left(F+\sqrt{G^2+F^2}\right)\right)\Big|_{z_1}^{z_2},$$
$$B_2 = B_1\cos\beta,\quad B_3 = B_1\sin\beta \quad \text{(A.10)}$$

References

[1] F. Königsberger, A.J.P. Sabberwal, An investigation into the cutting force pulsations during milling operations, International Journal of Machine Tool Design and Research 1 (1961) 15–33.

[2] S. Jayaram, S.G. Kapoor, R.E. DeVor, Estimation of the specific cutting pressures for mechanistic cutting force models, International Journal of Machine Tools and Manufacture 41 (1) (2001) 265–281.

[3] R. Zhu, S.G. Kapoor, R.E. DeVor, Mechanistic modeling of the ball end milling process for multi-axis machining of free-form surfaces, ASME Journal of Manufacturing Science and Engineering 123 (3) (2001) 369–379.

[4] I. Lazoglu, Sculpture surface machining: a generalized model of ball-end milling force system, International Journal of Machine Tools and Manufacture 43 (2003) 453–462.

[5] E. Budak, Y. Altintaş, E.J.A. Armarego, Prediction of milling force coefficients from orthogonal cutting data, ASME Journal of Manufacturing Science and Engineering 118 (2) (1996) 216–224.

[6] P. Lee, Y. Altintaş, Prediction of ball-end milling forces from orthogonal cutting data, International Journal of Machine Tools and Manufacture 36 (9) (1996) 1059–1072.

[7] G. Yücesan, Y. Altintaş, Prediction of ball end milling forces, ASME Journal of Engineering for Industry 118 (1) (1996) 95–103.

[8] T. Bailey, M.A. Elbestawi, T.I. El-Wardany, P. Fitzpatrick, Generic simulation approach for multi-axis machining, Parts 1 and 2, ASME Journal of Manufacturing Science and Engineering 124 (3) (2002) 624–642.

[9] S. Engin, Y. Altintaş, Mechanics and dynamics of general milling cutters. Part I: Helical end mills, International Journal of Machine Tools and Manufacture 41 (15) (2001) 2195–2212.

[10] Y. Altintaş, P. Lee, Mechanics and dynamics of ball end milling, ASME Journal of Manufacturing Science and Engineering 120 (4) (1998) 684–692.